INPOP21a planetary ephemerides

A. Fienga[1,2], P. Deram[1], A. Di Ruscio[1,3], V. Viswanathan[1,5,6], J.I.B. Camargo[4], L. Bernus[2], M. Gastineau[2], J. Laskar[2]

[1] Géoazur-CNRS 7329, Observatoire de la Côte d'Azur, Valbonne, France
[2] IMCCE-CNRS 8028, Observatoire de Paris, Paris, France
[3] CRAS, University Sapienza, Rome, Italy
[4] Observatorio Nacional/MCTIC, Rio de Janeiro, Brazil
[5] CRESST II, University of Maryland, Baltimore, USA
[6] NASA Goddard Space Flight Center, Greenbelt, USA

Abstract

The major points of improvement of INPOP21a relative to INPOP19a are i) the addition of 2 years of Mars Express data and 1 year of Juno normal points, ii) the use of new Uranus ground-based optical observations reduced with the Gaia DR3, iii) the modification of the dynamical modeling for the Kuiper belt object perturbations, and iv) the first determination of the Sun oblateness including the Lense-Thirring effect.

1 Improvement of the dynamical modeling

1.1 Kuiper belt objects

In INPOP19a, a modeling based on a three circular rings representing the perturbations of objects located at 39.4, 44.0 and 47.5 AU has been introduced. With this modeling, the impact of the eccentricity of TNO orbits was not including in the computation of the accelerations induced by the TNO on the planet orbits. Furthermore, the global mass of these rings appears to be quite large in comparisons to theoretical estimations and as TNO orbits tend to be more eccentric compared to main belt asteroids, we implement an alternative representation of the TNO perturbations by considering directly observed orbits extracted from the *Astorb* database. Orbits are supposed to be in the ecliptic, with zero inclination. On the total of 2225 objects with semi-major axis between 39.3 and 47.6 AU, we performed random selections of 500 that we integrated as individual objects with the same mass spread over the 500. Thanks to this approach the representation of the TNO is more realistic as one can see on Fig. 1, in particular, regarding the distributions in eccentricities (Panel C of Fig. 2) and in semi-major axis (Panel B of Fig. 2). For each random sampling of 500 objects, a full fit was made, adjusting in addition to the regular planetary ephemerides parameters, the global mass of the 500. Results being very similar from one random selection to another, one selection was chosen arbitrary for the rest of this study.

After fit, the global mass for 500 TNOs is found to be (0.0259 ± 0.0007) $M_\oplus$. This mass is about two times smaller than the one proposed by [3], (0.061±0.001) $M_\oplus$, but still higher than the one obtained by [11], (0.0111±0.0025)$M_\oplus$. These differences can be explained first by the differences in the dynamical modeling between this work and [3]. Where in [3] circular rings were used, we include here a real distribution of orbits with various eccentricities as one sees on Fig. **??**. Because of the eccentric orbits inducing variations in the mean distances between planets and TNOs, it was expected than the global mass of the TNO ring to be smaller than the one obtained with circular rings. Furthermore, as it is also shown on Fig. 1, in terms of semi-major axis, the distribution of the *Astorb* orbits is also different from the one considered in INPOP19a (see. Fig. 2 and 3). Both arguments explain the deduced smaller mass for the TNO ring.

1.2 Lense-Thirring

When comparing INPOP previous Sun oblateness estimations with those obtained from helioseismology, it is important to keep in mind that an additional contribution must be included in order to compare two consistent estimates: the effect of the Sun rotation of the space-time metric. This effect known as the Lense-Thirring effect, has been evaluated to contribute to about 10% of the dynamical acceleration induced by the shape of the Sun. The acceleration induced by the Lense-Thirring effect
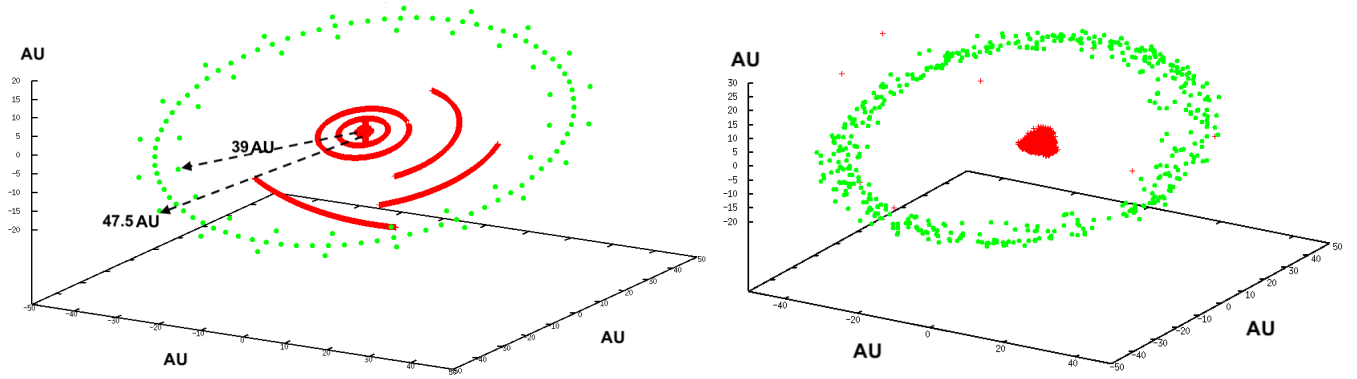
Figure 1: Comparison between the INPOP19a TNO modeling and one selection of 500 orbits randomly chosen from the *Astorb* database in cartesian coordinates centered on the Solar System Barycenter.
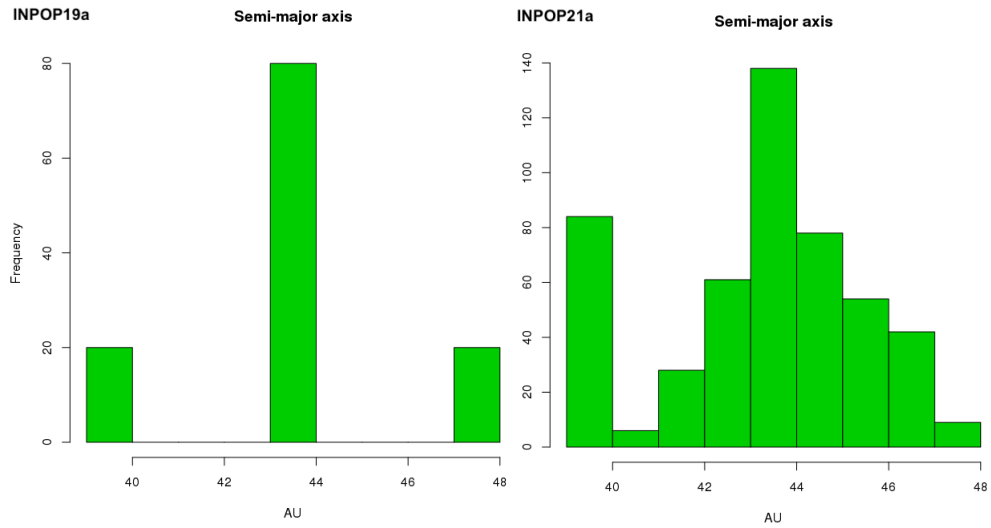

Figure 2: Semi-major axis distributions: Comparison between the INPOP19a TNO modeling and one selection of 500 orbits randomly chosen from the *Astorb* database.
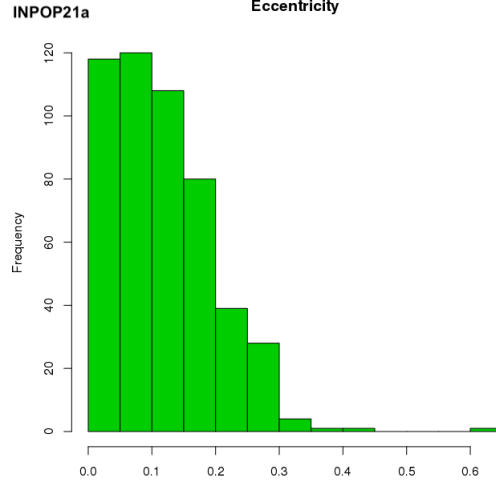
Figure 3: Distribution in eccentricities for INPOP21a TNO modeling and one selection of 500 orbits randomly chosen from the *Astorb* database. In INPOP19a, the TNO rings were circular.

generated by a central body (at first post-Newtonian approximation) is given by

$$\mathbf{a}_{LT} = \frac{(\gamma + 1)G}{c^2 r^3} S \left[3 \frac{\mathbf{k}.\mathbf{r}}{r^2} (\mathbf{r} \wedge \mathbf{v}) - (\mathbf{k} \wedge \mathbf{v}) \right] \tag{1}$$

where $\mathbf{S}$ is the Sun's angular momentum such as $\mathbf{S} = S\mathbf{k}$ where $\mathbf{k}$ is the direction of the Sun's rotation pole defined as per the IAU right ascension and declinaison ([2]), $\mathbf{r}$ and $\mathbf{v}$ are the position and velocity vectors of the planet relative to the central body (here the Sun) and γ is the Post-Parametrized Newtonian (PPN) parameter for the light deflection. Depending on the rotation of the Sun's core, one can estimate different values for the amplitude of the Sun's angular momentum $\mathbf{S}$ which are then tested and presented in Table 1.

The value obtained for INPOP21a is given in the first line of Table 1. The obtained value is very close to the values deduced from SOHO $(2.22 \pm 0.009) \times 10^{-7}$ and GONG $(2.18 \pm 0.005) \times 10^{-7}$ proposed by [1]. Furthermore, by considering the weighted average of these two values, which is $(2.206 \pm 0.007) \times 10^{-7}$, one finds an even better match with our estimation, $(2.2180 \pm 0.010) \times 10^{-7}$. It is also in good agreement with the previous analysis of the same data made by [10] giving an average estimate between GONG and SOHO, $(2.18 \pm 0.06) \times 10^{-7}$.

2   Update of the data sample

Table 3 gives the weighted root mean squares (WRMS) of the postfit residuals obtained with IN-POP21a and INPOP19a.

2.1   Mars

With INPOP19a, the Mars Express data were counted up to mid-2017. In INPOP21a, we add a additional years up to 2019.7. The same list modeling of main-belt asteroid perturbation is used in INPOP19a and INPOP21a as well as the same constraints on the asteroid densities (see [4]).

Table 1: Are given in Column 3, the values of Sun J2 obtained after fit using the values of the amplitude of the angular momentum given in Column 2. Values deduced from helioseismology are extracted from [1] and [10]

Type of rotation	S $\times 10^{48}$ g.cm^{-2}.s^{-1}	J2 $\times 10^7$
INPOP21a with LT	1.90 ± 1.5	2.2180 ± 0.01
[9]	1.96 ± 0.7	2.28 ± 0.06
[10]		2.1800 ± 0.06
[1]		2.2057 ± 0.007

Table 2: Values of parameters obtained in the fit of INPOP21a, INPOP19a, INPOP17a observations. The values from DE440 are taken from [9]

	INPOP21a ± 1σ	INPOP19a ± 1σ	INPOP17a ± 1σ	DE440
(EMRAT-81.3000)$\times 10^{-4}$	(5.678 ± 0.0095)	(5.668 ± 0.010)	5.719 ± 0.010	
GM$_\odot$ - 132712440000 [km^3. s^{-2}]	(41.8453 ± 0.11)	(42.0322 ± 0.13)	(42.693 ± 0.04)	41.27942
TNO mass [M$_\oplus$]	(0.0259 ± 0.0007)	(0.061 ± 0.001)	NA	

2.2 Jupiter

With INPOP21a, we extend the Juno data sample from 2018.7 to 2020.56 thanks to CRAS delivery. These additional normal points were deduced from the jovian perijove PJ25 and PJ28. See [5] for more explanation.

2.3 Uranus

In [6], a new reduction of astrometric long-term observations of the Uranian main satellites obtained at the Pico dos Dias from 1982 to 2011, using the Gaia EDR3 [?] as reference, have been determined and will be published soon. For INPOP21a, we replace their old observations, already included in INPOP19a, by the positions obtained from the new reduction.

2.4 Moon

The LLR data were extended to 2020/06/01 totaling 27899 normal points. The Earth Orientation Parameters from the KEOF COMB2019 solution [12] have been used for reducing the LLR data. Results of the Moon adjustment are presented in Tables 4, 5, 6, 7, 8 and Fig. 10; where LLR 1-way range wrms (in cm), labelled LWRMS, is computed as $LWRMS = 0.5 \times \sqrt{\frac{\sum((O_i - C_i)^2/w_i^2)}{\sum(1/w_i^2)}}$, with O and C as observed and calculated 2-way range with weight w for each normal point i.

Table 3: INPOP21a data samples. Column 1 gives the observed planet and information on the type of observations, Column 2 gives the labels used on Fig. 4 and Column 3 indicates the number of observations. Columns 4 and 5 give the time interval and the a priori uncertainties provided by space agencies or the navigation teams, respectively. Finally, the WRMS for INPOP19a and INPOP21a are given in the last two columns.

| Planet / Type		Number	Period	*a prior* Accuracy	WRMS INPOP19a	WRMS INPOP21a
Mercury						
Direct range [m]	1:radar	462	1971.29 : 1997.60	900	0.95	0.95
Messenger range [m]	1:MSG	1096	2011.23 : 2014.26	5	0.82	0.82
Mariner range [m]		2	1974.24 : 1976.21	100	0.37	0.42
Venus						
VLBI [mas]	2:VLBI	68	1990.70 : 2013.14	2.0	1.13	1.15
Direct range [m]	2:radar	489	1965.96 : 1990.07	1400	0.98	0.98
Vex range [m]	2:Vex	24783	2006.32 : 2011.45	7.0	0.93	0.94
Mars						
VLBI [mas]	4:VLBI	194	1989.13 : 2013.86	0.3	1.26	1.26
Mex range [m]	4:Mex3	34118	2005.17 : 2019.37	2.0	2.47	1.09
	4:Mex2	30669	2005.17 : 2017.37	2.0	0.98	1.06
	4:Mex1		2005.17 : 2016.37	2.0	0.97	1.01
MGS range [m]	4:MGS	2459	1999.31 : 2006.70	2.0	0.93	0.94
MRO/MO range [m]	4:MRO/MO	20985	2002.14 : 2014.00	1.2	1.07	1.02
Jupiter						
VLBI [mas]	5:VLBI	24	1996.54 : 1997.94	11	1.01	1.0
Optical RA/Dec [arcsec]	5:Opt	6416	1924.34 : 2008.49	0.3	1.0	1.015
Flyby RA/Dec [mas]	5:FlybyRD	5	1974.92 : 2001.00	8.0	0.97	0.99
Flyby range [m]	5:Flyby	5	1974.92 : 2001.00	2000	0.98	1.24
Juno range [m]	17:Juno2	14	2016.65 : 2020.56	20	1.4	0.96
	5:Juno	9	2016.65 : 2018.68	20	0.945	0.87
Saturn						
Optical RA/Dec [arcsec]	6:Opt	7826	1924.22 : 2008.34	0.3	0.915	0.91
Cassini						
VLBI RA/Dec [mas]	6:VLBI	10	2004.69 : 2009.31	0.6	0.98	0.96
JPL range [m]	6:JPL	165	2004.41 : 2014.38	25.0	0.99	1.03
Grand Finale range [m]	6:GF	9	2017.35 : 2017.55	1.0	1.71	0.8
Navigation [m]	6:Nav	572	2006.01 : 2009.83	6.0	0.71	0.85
		230	2006.01 :2006.5	6.0		0.85
		342	2008.96 : 2009.83	3.0		1.13
TGF range [m]	6:Nav	42	2006.01 : 2016.61	15.0	1.13	1.30
Uranus						
Optical RA/Dec [arcsec]	7:Opt2	22252	1924.62 : 2013.75	0.25	1.57	1.01
	7:Opt	12893	1924.62 : 2011.74	0.25	1.17	1.18
Flyby RA/Dec [mas]		1	1986.07 : 1986.07	50	0.32	0.25
Flyby range [m]		1	1986.07 : 1986.07	50	0.92	0.92
Neptune						
Optical RA/Dec [arcsec]	8:Opt	5254	1924.04 : 2007.88	0.3	1.0	0.92
Flyby RA/Dec [mas]		1	1989.65 : 1989.65	15.0	0.12	0.12
Flyby range [m]		1	1989.65 : 1989.65	2	1.14	3.7
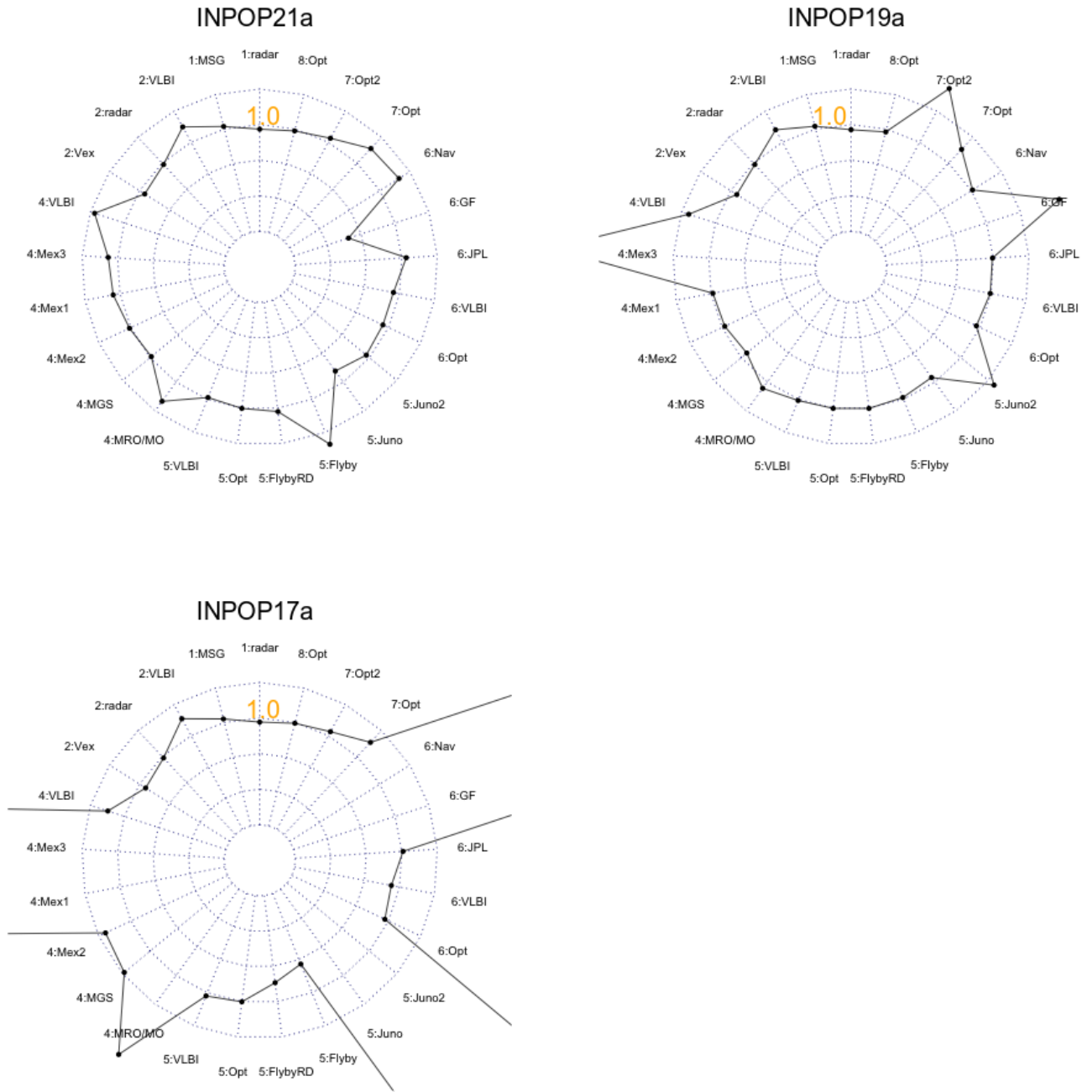
Figure 4: WRMS for INPOP21a, INPOP19a, INPOP17a. The labels correspond to the second column of Table 3 .
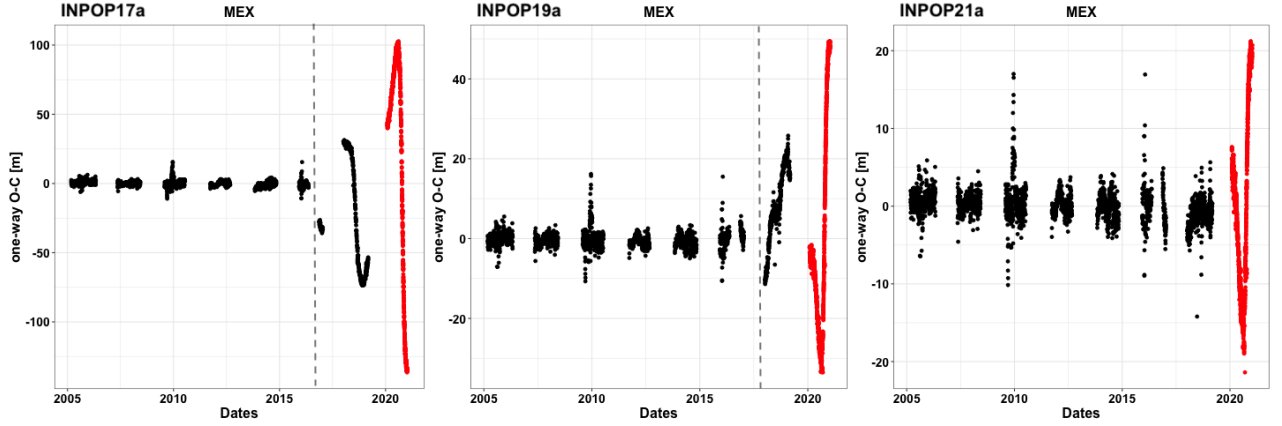
Figure 5: MEX postfit and extrapolation residuals for INPOP21a, INPOP19a, INPOP17a. The red plots indicate extrapolations residuals common to the three ephemerides when the dash line indicates the end of the fitting interval for INPOP19a and INPOP17a.

3   Results

3.1   Postfit residuals and extrapolation: Comparisons with INPOP19a and IN-POP17a

On Table 3 and Figure 4 are given the WRMS for INPOP21a, INPOP19a and INPOP17a. The WRMS here is defined as $WRMS = \sqrt{\sum \frac{((O_i - C_i)^2}{\sigma_i^2}}$, where $(O - C)_i$ is the postfit residual for the observation i, σ_i is the *a priori* instrumental uncertainty of the observation i given in Column 5 of Table 3.

We recall that a value of 1 for the WRMS indicates a perfect accordance between the adjustment and the expected accuracy of each of the data sets. By comparing the three radar charts of Figure 4, one can see the improvement brought by each version relative to the new implemented data sets without degrading the residuals of the other data sets.

Regarding Saturn, one can note the slightly over-fitting of the Cassini Grand Final observations (labelled 6:GF) with INPOP21a. This can be explained by very small number of normal points (9) obtained during the final phase of the mission, and consequently the sensitivity of the 6GF WRMS to the fit.

Concerning Jupiter, we can note the degradation of the Jupiter flyby residuals with INPOP21a relative to the INPOP19a or INPOP17a residuals. This can be explained by the 2 years prolongation of the Juno data sample between INPOP21a and INPOP19a. One can notice that INPOP17a residuals for Juno were off the radar chart as they were of about 100 times the expected accuracies.

For Mars, we still note a degradation of the INPOP19a and INPOP17a extrapolation out from their fitting intervals (4:Mex3 and 4:Mex2), even if as one can see on Figure 5, the degradation of the extrapolation tends to reduce. When for INPOP17a the speed of degradation was about 2.2 m per year the first year of extrapolation (2016:2017), 21 m per year over the period 2017:2019 and 18 m per year over the period 2019:2021. For INPOP19a it is of about 5 m per year over the period 2017:2019 and 14 m per year over the period 2019:2021. With INPOP21a the degradation is about 6 m per year over the period 2019:2021.

9

Finally, 7:Opt2 indicates the WRMS for the updated Uranus data samples from [6]. Despite good residuals with INPOP17a, one can notice a degradation of these residuals with INPOP19a, corrected with INPOP21a.

It will be interesting to test the extrapolation capabilities for Uranus and Neptune by comparison with recently reduced or obtained satellite positions analysed using the Gaia DR3 catalog. Thanks to Gaia, it is now possible to detect planetary ephemerides bias too small to be clearly identified a ephemerides bias because of the uncertainties and zonal errors of the previous stellar catalogs. In this sense we expect a lot from Gaia DR3 re-reduction of Neptune satellite observations.

3.2   Comparisons with DE438 and DE440

On Figs 6, 7, 8, 9 are plotted the heliocentric differences in longitude, latitude and distances between DE438 and INPOP19a and between DE440 and INPOP21a for all the planets. For the eight planets, the differences between INPOP21a and DE440 (in red) are smaller than the differences between DE438 and INPOP19a (in black). This tends to show a convergence of the DE and INPOP models.

For Mars, the differences to DE440 are systematically smaller than the one between INPOP (19a or 21a) and DE438. Furthermore the amplification of the distance differences clearly visible with DE438 tends to disappear with DE440 in favor of period signature with constant amplitude. For the longitudes and latitudes, the differences are also reduced when considering DE440-INPOP21a. For the Earth the reduction of the differences between DE440 and INPOP21a are more clearly visible for the latitude than for the longitude or the distances. This comment is also true for Venus and Mercury.

For Jupiter, there is a clear offset between DE ephemerides and INPOP21a. This offset is due to the value of the transponder delay that has been chosen for the JPL solutions that differs from the one estimated by the CRAS team during their Juno radio science data analysis. As INPOP used the CRAS normal points for its construction, we have used the corresponding transponder delay. The offset is estimated to be about 150 m. Besides this offset, the dispersion of the DE-INPOP21a differences is clearly reduced in comparison with DE-INPOP19a, from about 180 m between DE438 and INPOP19a to 70 m from DE440 and INPOP21a over the period 1980:2040.

For Saturn, one can clearly see the interval of the Cassini data sample between 2004 and 2017 for which the agreement between the ephemerides is clear. Before and after this interval, the differences reach 1 km over 60 years. From the angular point of view, the differences remain below the mas level over the same period of time.This is significantly better than with the Jupiter angular differences that remain below the mas level. We can explain this result by the use of the Cassini VLBA tracking data [7], labelled 6:VLBI in Fig 4 and Table 3. By the duration of the sample (from 2004 to 2014 in [7] and up to end of the mission in [8]) and the sub-mas accuracy of the Saturn barycenter positions, this sample gives a strong constraint to the Saturn orbit.

For Uranus and Neptune the differences in Longitudes and Latitudes remain below the accuracies of the optical observations (below 100 mas during the 1980:2010 period).

References

[1] H. M. Antia, S. M. Chitre, and D. O. Gough. Temporal variations in the Sun's rotational kinetic energy. A&A, 477(2):657–663, January 2008.

Figure 6: Differences between INPOP19a and INPOP21a and between DE438 (red curves) and DE440 (black curves) in Heliocentric coordinates and distances for Mercury and Venus.

Figure 7: Differences between INPOP19a and INPOP21a and between DE438 (red curves) and DE440 (black curves) in Heliocentric coordinates and distances for Mars and Earth.

Figure 8: Differences between INPOP19a and INPOP21a and between DE438 (red curves) and DE440 (black curves) in Heliocentric coordinates and distances for Jupiter and Saturn.
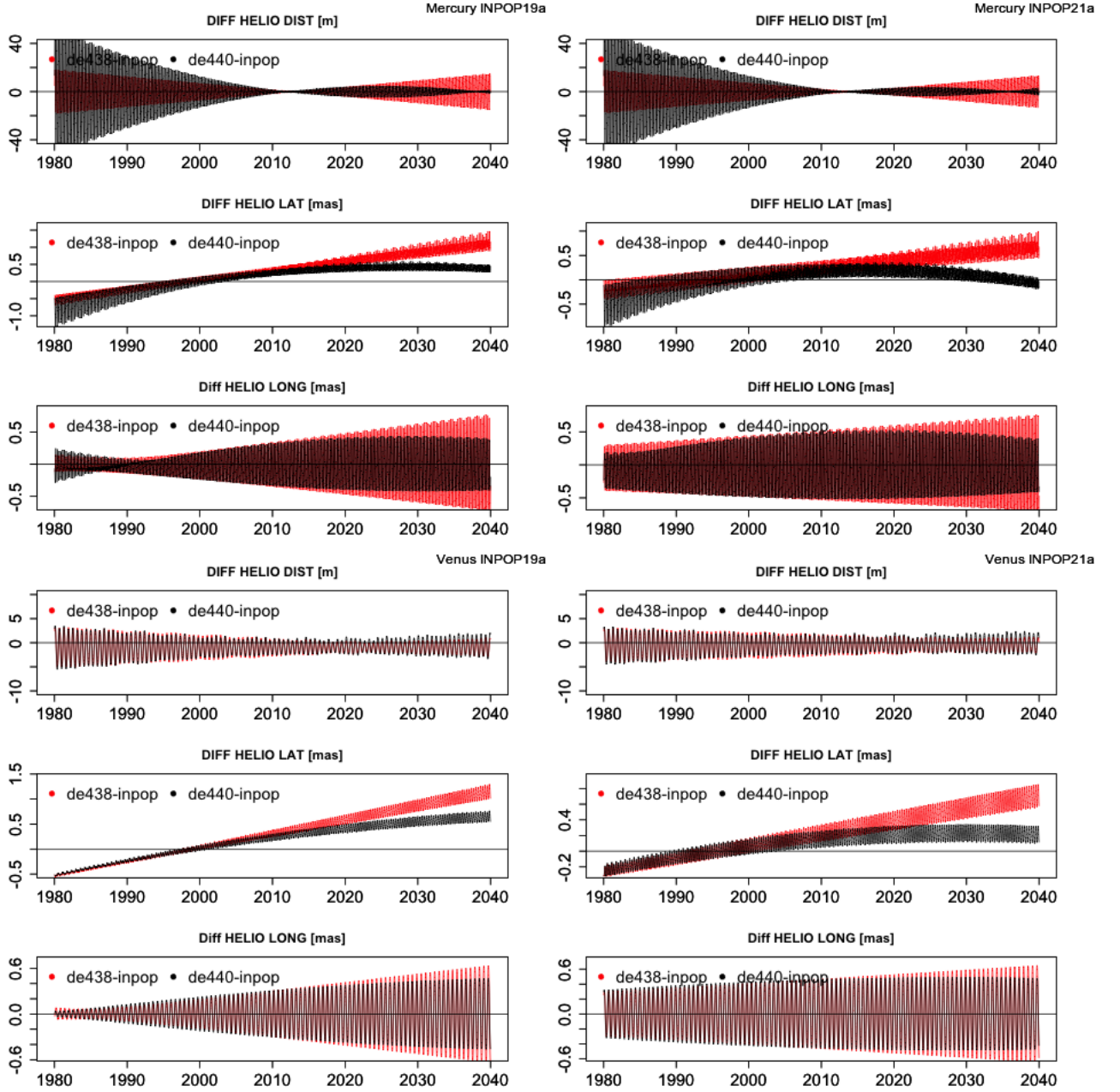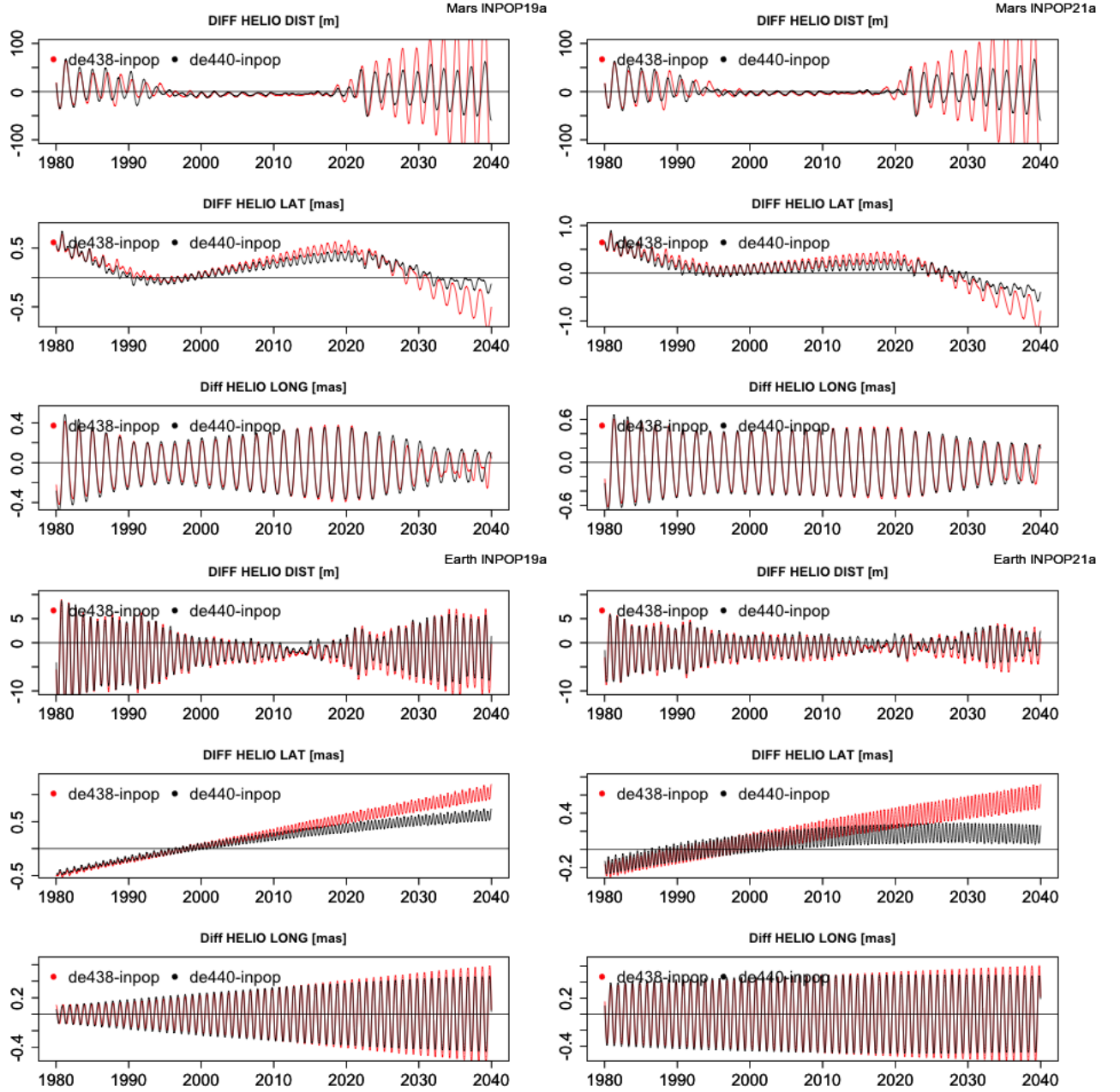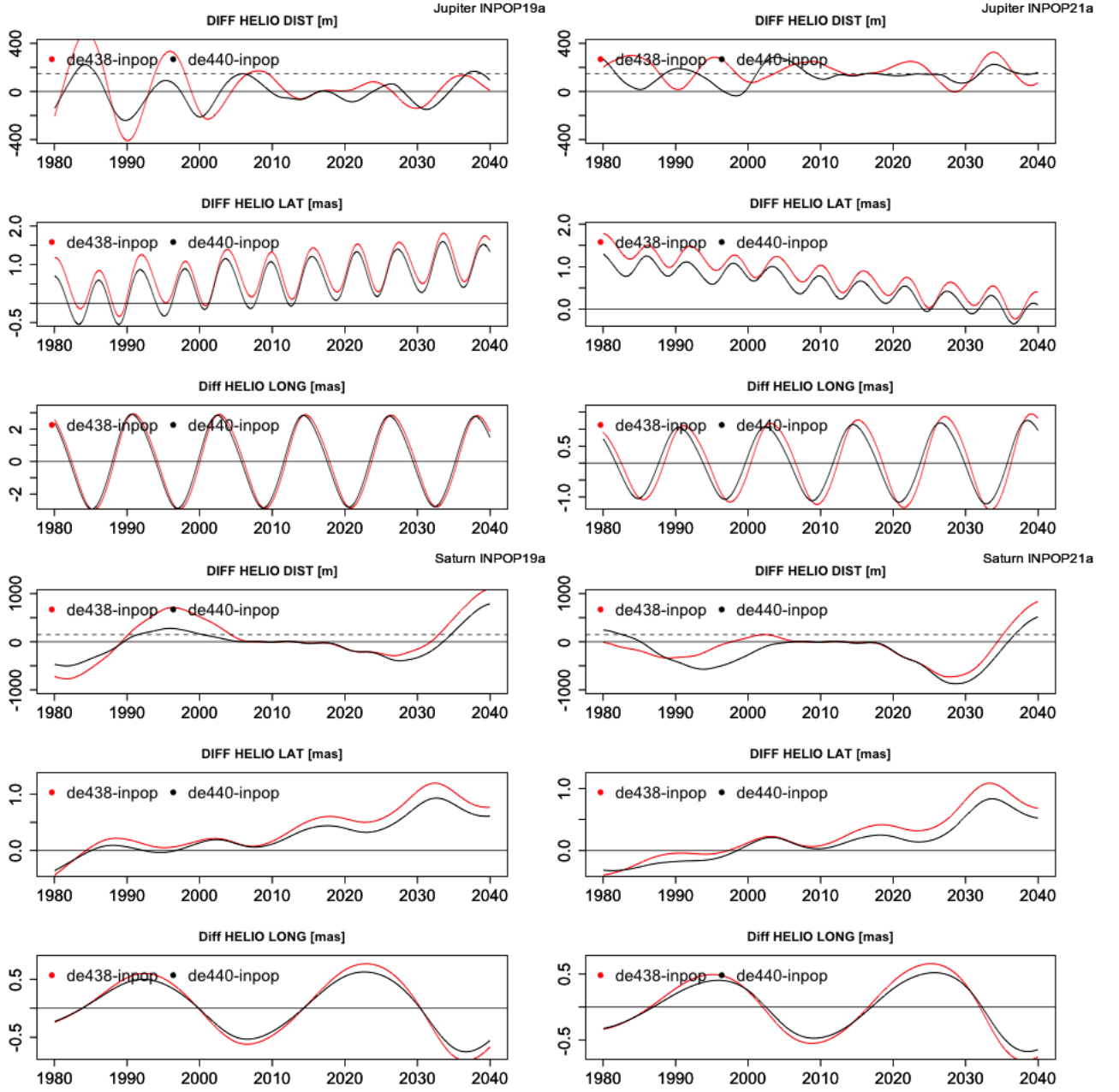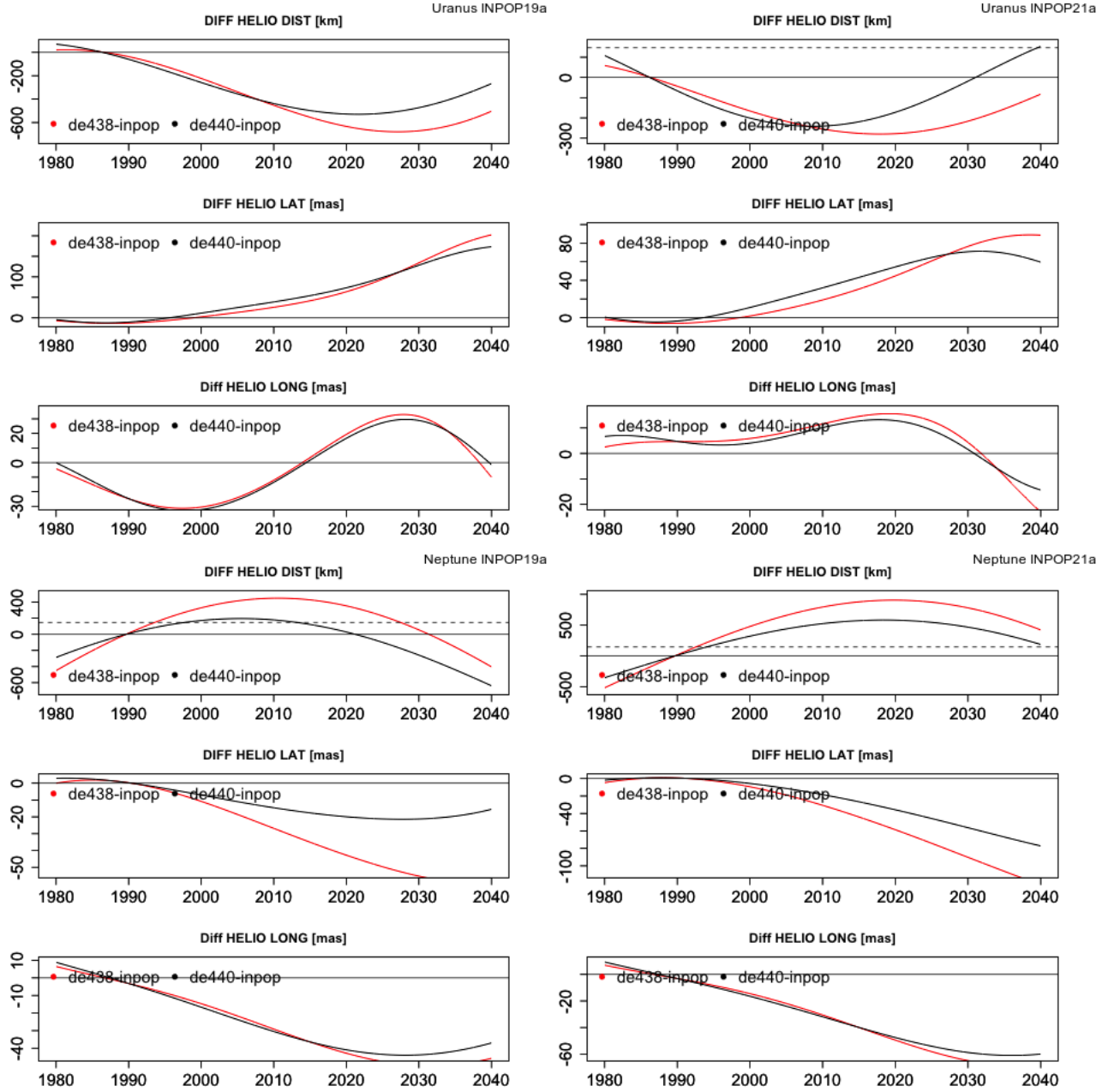
Figure 9: Differences between INPOP19a and INPOP21a and between DE438 (red curves) and DE440 (black curves) in Heliocentric coordinates and distances for Uranus and Neptune.

Table 4: Post-fit residuals (LWRMS in cm) of LLR observations

Station	Time span	INPOP21a Used	INPOP21a LWRMS
APOLLO	2006-2010	929	1.26
APOLLO	2010-2012	496	1.75
APOLLO	2012-2013	347	1.41
APOLLO	2013-2016	816	1.06
Grasse	1984-1986	1095	14.03
Grasse	1987-1995	3275	4.67
Grasse	1995-2006	4854	3.02
Grasse	2009-2013	981	1.33
Grasse	2013-2017	3428	1.07
Grasse	2017-2020	3458	1.01
Haleakala	1984-1990	737	5.96
Matera	2003-2013	37	2.01
Matera	2013-2015	27	2.42
Matera	2015-2020	169	2.51
McDonald	1969-1983	3276	18.48
McDonald	1983-1986	155	14.09
MLRS1	1983-1984	44	31.18
MLRS2	1984-1985	347	54.80
MLRS2	1985-1989	207	17.82
MLRS2	1988-1997	1189	4.01
MLRS2	1997-2013	1936	3.20
MLRS2	2013-2016	15	2.39
Wettzell	2018-2020	81	0.79

Table 5: Parameters for the Earth-Moon system.

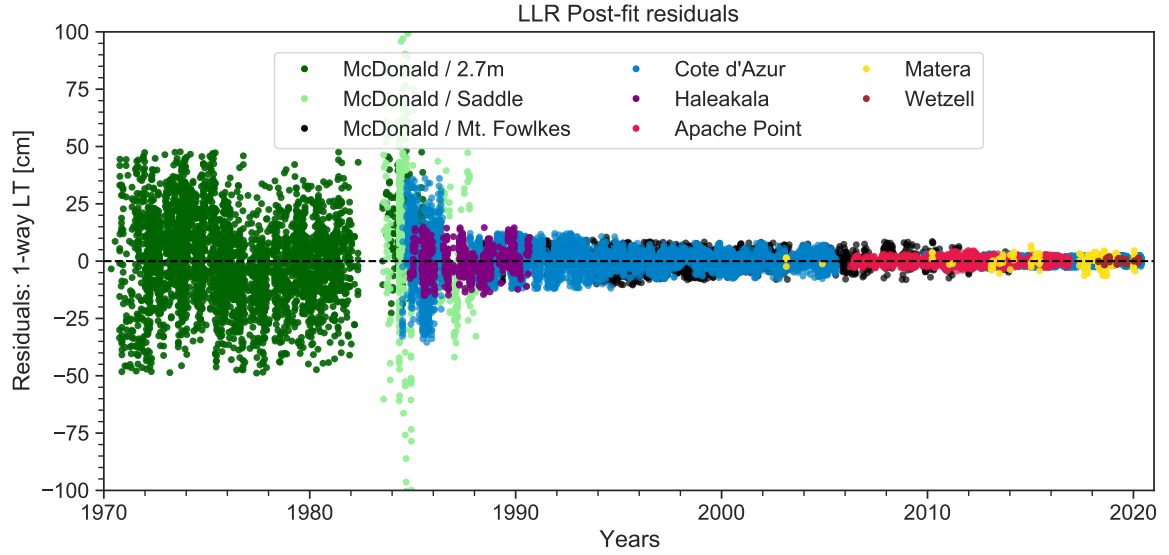| Parameter	Units	INPOP19a	INPOP21a
GM_{EMB}	au^3/d^2	8.997011394E-10	8.997011395E-10
$\tau_{R1,E}$	d	7.98E-03	8.02E-3
$\tau_{R2,E}$	d	2.82E-03	2.82E-03
$C_T/(MR^2)$		3.93140E-01	3.93141E-01
C_{32}		4.84500E-06	4.84501E-06
S_{32}		1.685E-06	1.685E-06
C_{33}		1.6686E-06	1.6689E-06
τ_M	d	9.4E-02	9.6E-02
k_v/C_T	d^{-1}	1.64E-08	1.62E-08
f_c		2.8E-04	2.8E-04
h_2		4.26E-02	4.23E-02

Figure 10: LLR post-fit residuals obtained with INPOP21a (LWRMS in cm) from 1969 to 2020.

Table 6: Amplitudes of periodic terms as corrections to longitude librations (in mas) obtained between ephemeris solutions to account for frequency-dependent dissipation in the Moon, where the polynomial expansion of the Delaunay arguments l' (solar mean anomaly), l (lunar mean anomaly), F (argument of latitude) and D (mean elongation of the Moon from the Sun) follow Eqn. 5.43 in **?**].

Parameter	Period (d)	Longitude libration correction (in mas)	
		INPOP19a	INPOP21a
$A_1 \cos(l')$	365.26	4.4	4.5 ± 0.2
$A_2 \cos(2l - 2D)$	205.89	1.7	1.8 ± 0.3
$A_3 \cos(2F - 2l)$	1095.22	9.7	10.5 ± 4.5

Table 7: Station and lunar surface reflector coordinates used for INPOP21a solution.

Earth Station	x	y	z	$\dot{x}$	$\dot{y}$	$\dot{z}$
APOLLO	-1463998.9079	-5166632.7663	3435012.8921	-0.0139	-0.0003	-0.0023
Grasse	4581692.1686	556196.0742	4389355.1225	-0.0151	0.0193	0.0114
Haleakala	-5466003.7272	-2404425.9189	2242197.8916	-0.0122	0.0622	0.0310
Matera	4641978.8100	1393067.5310	4133249.4800	-0.0180	0.0192	0.0140
McDonald	-1330781.6134	-5328756.4702	3235697.8262	-0.0244	-0.0319	0.0091
MLRS1	-1330121.0057	-5328532.3595	3236146.0225	-0.0124	0.0009	-0.0053
MLRS2	-1330021.1222	-5328401.8695	3236480.7584	-0.0121	0.0015	-0.0036
Wettzell	4075576.7721	931785.5248	4801583.5601	-0.0139	0.0170	0.0124

Lunar reflector coordinates (in INPOP21a PA frame)	x	y	z			
Apollo 11	1591966.6407	690699.4669	21003.7578			
Lunokhod 1	1114292.2303	-781298.4355	1076058.6227			
Apollo 14	1652689.5625	-520997.5929	-109730.5181			
Apollo 15	1554678.3071	98095.5262	765005.2077			
Lunokhod 2	1339363.3937	801871.9437	756358.6633			

[2] B. A. Archinal, C. H. Acton, M. F. A'Hearn, A. Conrad, G. J. Consolmagno, T. Duxbury, D. Hestroffer, J. L. Hilton, R. L. Kirk, S. A. Klioner, D. McCarthy, K. Meech, J. Oberst, J. Ping, P. K. Seidelmann, D. J. Tholen, P. C. Thomas, and I. P. Williams. Report of the IAU Working Group on Cartographic Coordinates and Rotational Elements: 2015. Celestial Mechanics and Dynamical Astronomy, 130(3):22, February 2018.

[3] A. Di Ruscio, A. **Fienga**, D. Durante, L. Iess, J. Laskar, and M. Gastineau. Analysis of Cassini radio tracking data for the construction of INPOP19a: A new estimate of the Kuiper belt mass. A&A, 640:A7, August 2020.

[4] A. **Fienga**, C. Avdellidou, and J. Hanuš. Asteroid masses obtained with INPOP planetary ephemerides. MNRAS, 492(1):589–602, February 2020.

[5] A. Fienga, P. Deram, V. Viswanathan, A. Di Ruscio, L. Bernus, D. Durante, M. Gastineau, and J. Laskar. INPOP19a planetary ephemerides. Notes Scientifiques et Techniques de l'Institut de Mecanique Celeste, 109, December 2019.

[6] J.I.B. Camargo et al. The five largest satellites of Uranus: 29 years of astrometric observations at the Pico dos Dias Observatory - to appear in MNRAS. 2021.

[7] Dayton L. Jones, William M. Folkner, Robert A. Jacobson, Christopher S. Jacobs, Vivek Dhawan, Jon Romney, and Ed Fomalont. Astrometry of Cassini With the Vlba to Improve the Saturn Ephemeris. AJ, 149(1):28, January 2015.

[8] Dayton L. Jones, William M. Folkner, Robert A. Jacobson, Christopher S. Jacobs, Jonathan Romney, and Vivek Dhawan. Very Long Baseline Array Astrometry of Cassini: The Final Epochs and an Improved Orbit of Saturn. AJ, 159(2):72, February 2020.

Table 8: Estimated values of station biases over different periods (2-way light time in cm).

| Bias # | Station | Date | Bias 2-way light time [cm] | |
			INPOP19a	INPOP21a
1	APOLLO	2006/04/07 - 2010/11/01	0.27	0.03
2		2007/12/15 - 2008/06/30	-3.95	-3.93
3		2008/09/20 - 2009/06/20	3.22	3.22
4		2010/11/01 - 2012/04/07	-6.03	-6.28
5		2012/04/07 - 2013/09/02	8.99	8.85
6	Grasse	1984/06/01 - 1986/06/13	16.99	17.12
7		1987/10/01 - 2005/08/01	-5.00	-5.41
8		1993/03/01 - 1996/10/01	9.36	9.81
9		1996/12/10 - 1997/01/18	14.04	14.32
10		1997/02/08 - 1998/06/24	20.39	20.79
11		2004/12/04 - 2004/12/07	-5.28	-5.53
12		2005/01/03 - 2005/01/06	-4.38	-4.53
13		2009/11/01 - 2014/01/01	-0.94	-0.99
14		2015/12/20 - 2015/12/21	-88.05	-88.05
15	Haleakala	1984/11/01 - 1990/09/01	9.54	10.07
16		1984/11/01 - 1986/04/01	-1.84	-0.72
17		1986/04/02 - 1987/07/30	9.52	9.81
18		1987/07/31 - 1987/08/14	2.57	1.86
19		1985/06/09 - 1985/06/10	-11.03	-11.18
20		1987/11/10 - 1988/02/18	17.32	18.57
21		1990/02/06 - 1990/09/01	11.68	13.36
22	Matera	2003/01/01 - 2016/01/01	0.06	0.34
23	McDonald	1969/01/01 - 1985/07/01	-45.21	-46.56
24		1971/12/01 - 1972/12/05	38.03	40.23
25		1972/04/21 - 1972/04/27	130.6	129.56
26		1974/08/18 - 1974/10/16	-116.54	-114.07
27		1975/10/05 - 1976/03/01	26.68	26.87
28		1983/12/01 - 1984/01/17	-3.94	-12.80
29		1969/01/01 - 1971/12/31	2266.53	2268.49
30	MLRS1	1983/08/01 - 1988/01/28	12.89	14.42

[9] Ryan S. Park, William M. Folkner, Alexander S. Konopliv, James G. Williams, David E. Smith, and Maria T. Zuber. Precession of Mercury's Perihelion from Ranging to the MESSENGER Spacecraft. AJ, 153(3):121, March 2017.

[10] Frank P. Pijpers. Helioseismic determination of the solar gravitational quadrupole moment. MNRAS, 297(3):L76–L80, July 1998.

[11] E. V. Pitjeva and N. P. Pitjev. Mass of the Kuiper belt. Celestial Mechanics and Dynamical Astronomy, 130(9):57, Sep 2018.

[12] James Ratcliff and R Gross. Combinations of Earth Orientation Measurements: SPACE2019, COMB2019, and POLE2019. Technical report, 10 2020.